Research Square

Preprints are preliminary reports that have not undergone peer review.
They should not be considered conclusive, used to inform clinical practice,
or referenced by the media as validated information.

Numerical Investigation of Nanofluid Laminar Flow Conjugate Heat Transfer With Al2O3 and Cuo Nanoparticles

Ihssan Mohammed Ali Rashid RASHID
Konya Technical University
Ulaş ATMACA
suatmaca@ktun.edu.tr

Konya Technical University

Research Article

Keywords: Laminar flow, Conjugate heat transfer, Nanofluid, Al2O3, CuO, Numerical solution

Posted Date: September 25th, 2026

DOI: https://doi.org/10.21203/rs.3.rs-10931243/v1

License: This work is licensed under a Creative Commons Attribution 4.0 International License.
Read Full License

Additional Declarations: No competing interests reported.

NUMERICAL INVESTIGATION OF NANOFLUID LAMINAR FLOW CONJUGATE HEAT TRANSFER WITH AL_2O_3 AND CUO NANOPARTICLES

*Ihssan Mohammed Ali Rashid RASHID, Ulaş ATMACA**

Konya Technical University, Engineering and Natural Science Faculty, Mechanical Engineering Department, Konya, 42150, Türkiye
*Corresponding author;suatmaca@ktun.edu.tr

This study numerically examines transient conjugate heat transfer in laminar nanofluid flow, for Al_2O_3 and CuO nanoparticles in a thick-walled micropipe. A single-phase model captures the coupled conduction–convection process under a convective boundary condition on the downstream wall. The energy equations for both domains are solved by a finite-difference method, validated through grid-independence tests using the Grid Convergence Index. Seven key parameters are analyzed: Peclet and Brinkman numbers, wall thickness ratio, wall-to-fluid thermal conductivity and diffusivity ratios, Biot number, and nanoparticle concentration. Findings reveal that significant heat flux is concentrated in the upstream region due to axial conduction in both fluid and solid domains. Elevated Peclet numbers shorten the preheating length and expedite the transition to steady state. Nanofluids containing Al_2O_3 exhibit higher downstream bulk temperatures than CuO. Increased wall thickness and a higher wall-to-fluid thermal conductivity ratio prolong the thermal stabilization period and diminish interfacial heat flux. Viscous dissipation induces reverse heat transfer near the entrance when Brinkman numbers are positive. This investigation underscores the sensitivity of thermal development to nanofluid properties and wall characteristics, providing insights for the design of micro-scale thermal systems.

Keywords: Laminar flow, Conjugate heat transfer, Nanofluid, Al_2O_3, CuO, Numerical solution

Introduction

Nanofluids, which are engineered suspensions of nanoparticles in base fluids, have attracted significant attention due to their enhanced thermal properties, particularly thermal conductivity and heat transfer capabilities. Since their introduction by Choi [1], nanofluids have shown considerable promise in various applications, including microchannel cooling, heat exchangers, thermal management of electronics, and solar energy utilization. Aluminum oxide and copper oxide are among the most frequently studied nanoparticle materials, and their dispersion in water has led to substantial improvements in convective heat transfer [2] -[3].
Numerous experimental and numerical investigations have been undertaken to assess nanofluid performance under diverse flow regimes, geometries, and boundary conditions [3], [2, 4-7]. These studies underscore the critical role of thermophysical properties, especially thermal conductivity and viscosity models, in predicting nanofluid behavior in practical scenarios. Furthermore, several reviews highlight the increasing development of hybrid nanofluids and the growing reliance on computational fluid dynamics tools for modeling nanofluid systems [8].
Conjugate heat transfer, a phenomenon involving simultaneous conduction in solids and convection in fluids, is crucial for understanding thermal transport in micro-scale devices [9]. This is particularly true for laminar flows within microchannels or micropipes, where axial conduction within both fluid and solid domains can significantly influence temperature evolution. While axial conduction is often neglected in macroscale systems, its effect becomes significant in microscale configurations.
Nanofluid modeling is typically categorized into single-phase and two-phase approaches. The single-phase model, which treats the nanofluid as a uniform mixture with effective thermophysical properties, offers computational simplicity [10]. In contrast, the two-phase model accounts for the distinct phases of the base fluid and nanoparticles, including their relative motion and interactions, generally

providing higher accuracy, especially at higher nanoparticle concentrations [11]. Despite its simplicity, the single-phase model has demonstrated good agreement with experimental data under specific conditions and is widely adopted due to its computational efficiency. Most existing research focuses on boundary conditions characterized by constant heat flux or temperature. However, real-world applications often involve convective boundary conditions, especially in systems exposed to fluctuating ambient temperatures. Moreover, the combined influence of wall thickness, wall-to-fluid thermal property ratios, and nanoparticle concentration on conjugate heat transfer under such conditions remains less comprehensively explored. This study presents a numerical investigation of transient conjugate heat transfer within a laminar nanofluid flow inside a thick-walled micropipe, employing a convective boundary condition. Utilizing a single-phase model, the research analyzes the impact of key parameters—namely, Peclet number, Brinkman number, wall thickness ratio, wall-to-fluid thermal conductivity and diffusivity ratios, Biot number, and nanoparticle concentration—for nanofluids containing Al_2O_3 and CuO nanoparticles. This work builds upon previous study conducted under constant temperature boundary condition [12] and aims to deliver detailed insights relevant to the thermal design of micro-scale systems.

Results and Discussion

This study presents a numerical investigation into the laminar forced convection of two distinct nanofluids within a micropipe, considering seven key parameters: Peclet number, wall thickness ratio, d', wall to nanofluid thermal conductivity ratio (k_{wnf}), wall to nanofluid thermal diffusivity ratio (α_{wnf}), Brinkman number, Br, Biot number, Bi, and nanoparticle concentration, φ. Solutions were obtained for four different concentrations of both Al_2O_3 and CuO nanofluids. Figures 2 and 3 illustrate the transient axial temperature distributions for the inner wall and nanofluid bulk, respectively, for three specified concentrations (φ=1%, 4%, and 7%) under conditions of $Pe=5$ and 50, $Br=0$, $Bi=10$, $d'=0.6$, $k_{wnf}=10$, and $\alpha_{wnf}=1$. These figures facilitate a comparison of preheating lengths at different Peclet numbers. Observations indicate significant heat transfer in the upstream region, attributed to axial conduction in both the wall and nanofluid. An increased Peclet number leads to a reduced preheating length. Initially, inner wall temperatures exceed nanofluid bulk temperatures, with the preheating length extending axially over time. Both temperatures eventually approach an asymptotic value of 1 in the fully developed, steady-state region, with the time to reach steady state decreasing as the Peclet number rises. The influence of nanofluid concentration is subtle at early transient times, primarily noticeable near $x'=0$. CuO nanofluids exhibit higher temperatures than Al2O3 counterparts, an effect amplified by increased concentration due to the enhanced thermal conductivity of the nanofluid. The impact of concentration becomes more pronounced in the upstream region at steady state, where concentration lines maintain a consistent arrangement.

Figure 2 indicates that higher Peclet numbers lead to diminished axial conduction within the nanofluid, causing inner wall temperatures to converge. Consequently, temperature profiles separate based on concentration. In the downstream region, rapid radial heat transfer causes nanofluid concentration lines to approach each other. Lower nanofluid concentrations and aluminum oxide (Al_2O_3) exhibit higher temperatures in these locations. Figure 3 presents the axial distribution of nanofluid bulk temperature for two distinct Peclet numbers. At steady state, the influence of nanofluid concentration is more apparent in Figures 2 and 3, significantly affecting bulk fluid temperatures. In the downstream region, Al_2O_3 generally yields higher bulk temperatures than copper oxide for comparable concentrations, with lower concentrations correlating to higher temperatures. However, the converse is true in the upstream region. An increase in the nanofluid's thermal conductivity results in lower bulk and inner wall temperatures at any given transient time. Conversely, in the upstream region, higher thermal conductivity leads to increased temperatures. At steady state and in the downstream region, concentration lines converge. This convergence is attributable to the enhanced heat transfer capabilities of nanofluids, which generally improve with increased nanoparticle concentration and thermal conductivity [22, 23].

Figure 4 illustrates the transient radial temperature distribution for both the fluid and wall at three distinct axial positions. Temperature profiles initiate development in both upstream and downstream regions from the outset of the simulation. Wall temperatures exceed those of the nanofluid due to the wall's superior thermal conductivity. In the thermally developed section, all temperature values stabilize at 1. Figure 4 also presents two nanofluids at varying concentrations, revealing that concentration effects are more pronounced in the upstream region and follow a consistent pattern. At the heating section's inception, concentration lines show an inversion from the wall to the nanofluid side. Conversely, the influence of nanofluid concentration diminishes in the downstream region. As depicted in Figure 4.b, nanofluid concentrations have minimal impact initially, but CuO nanofluids demonstrate higher values over time, with greater concentrations leading to elevated temperatures.

The interfacial heat flux variation along the axial distribution is presented in Figure 5 for three different Peclet numbers. A decrease in the Peclet number significantly increases both the preheating length and the thermal development length, consequently extending the time required to reach steady state. The effect of nanofluid concentration is more evident at lower Peclet numbers, attributed to axial conduction. The sequence of concentrations remains consistent across all Peclet numbers and transient times in the downstream region. Increased thermal conductivity of the nanofluid correlates with lower interfacial heat flux values. Near the heating point ($x'=0$), concentration lines exhibit distortion and reversal on the wall side compared to the nanofluid side. Figure 5.c suggests that transient time lines and nanofluid concentration values are closely aligned due to the rapid movement of the nanofluid.

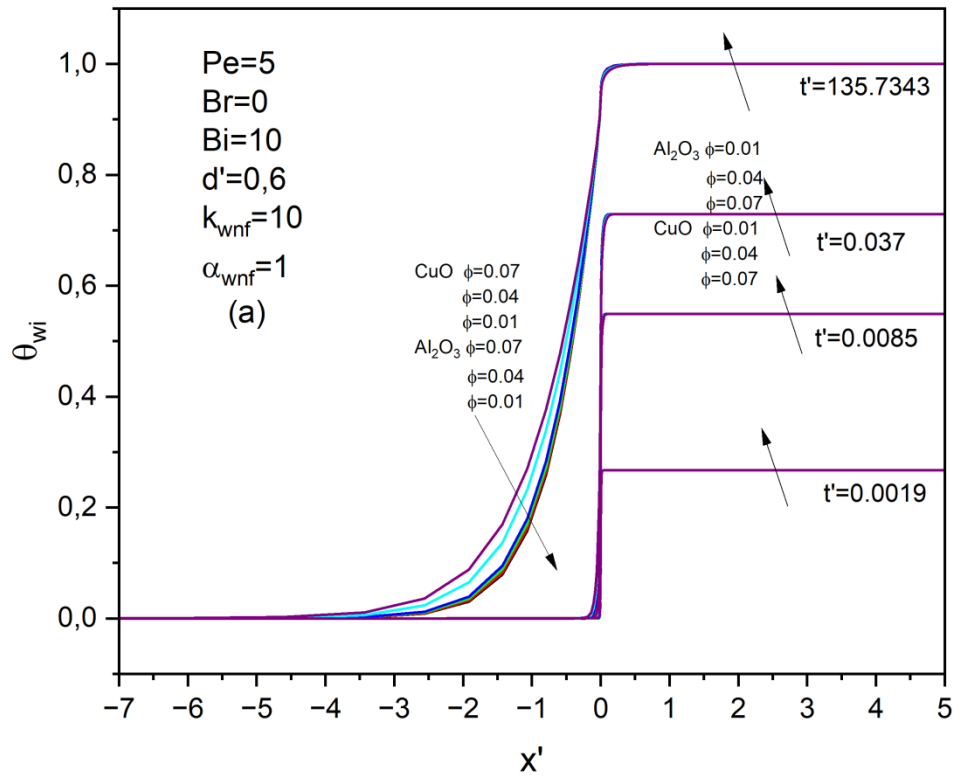
Figure 6 displays the axial distribution of interfacial heat flux for three distinct wall thickness ratios. Higher peak interfacial heat flux values are observed for thinner pipes, owing to reduced radial resistance and thermal capacity. An increase in wall thickness leads to a decrease in peak and interfacial heat flux values. The time required to achieve steady state also increases with greater wall thickness. The impact of nanofluid concentration is more clearly discernible in thicker pipes during the early transient periods, with the concentration sequence remaining consistent across all wall thickness ratios and transient times. In proximity to $x'=0$, the effect of nanofluid concentration is more apparent in thicker pipes. This observation underscores the significant role of wall thermal mass in modulating transient heat transfer characteristics and the interaction between the wall and the nanofluid. The thermal performance of nanofluids is intricately linked to their thermophysical properties, such as thermal conductivity, which are influenced by nanoparticle concentration and type [22].

The influence of the wall-to-nanofluid thermal conductivity ratio (k_{wnf}) on interfacial heat flux is illustrated in Figure 7 for three distinct k_{wnf} values. An increase in k_{wnf}, attributed to a higher thermal conductivity at the wall compared to the nanofluid, leads to a greater penetration length and enhanced reverse heat flux in the upstream region. The time required to attain a steady state also escalates with rising k_{wnf}. The impact of nanofluid concentration becomes more apparent at lower k_{wnf} values. While the sequence of concentration curves remains consistent for k_{wnf} values of 10 and 100, an inversion of concentration curves is observed at early transient times when $k_{wnf}=1$.

Figure 8 presents the effect of the wall-to-nanofluid thermal diffusivity ratio (α_{wnf}) on interfacial heat flux distribution. Lower α_{wnf} values result in higher peak and transient heat flux, a consequence of increased thermal inertia. Steady-state attainment time also lengthens as the thermal diffusivity ratio decreases. The arrangement of nanofluid concentration curves remains unchanged in both downstream and upstream regions, except for a localized reversal near $x'=0$. At higher α_{wnf} values and in the upstream region, nanofluid concentration values tend to converge. The duration to reach steady state increases with decreasing α_{wnf}, attributable to the nanofluid's thermal inertia. The variation in nanofluid concentration is not clearly discernible in the downstream region at steady state.

Figure 9 displays the axial distribution of interfacial heat flux over time for four different Brinkman numbers, examining the effects of viscous dissipation on heat transfer characteristics. Throughout all time steps, fluid temperatures in the upstream region rise with increasing viscous dissipation, and for positive Br numbers, a reverse heat flux from the fluid to the wall occurs. The upstream region values

are positive for all transient times, as anticipated. The time to reach a steady state does not exhibit significant changes. Positive Br numbers induce negative interfacial heat flux due to viscous heating within the nanofluid. The sequence of nanofluid concentrations shifts over time for Br=0.2. The impact of nanofluid concentration is more pronounced at higher Brinkman numbers in the upstream region, owing to viscous heating. Conversely, the influence of nanofluid concentration is evident at early transient times in the downstream regions but diminishes as time progresses. This highlights the complex interplay between viscous dissipation, nanofluid concentration, and transient heat transfer dynamics.



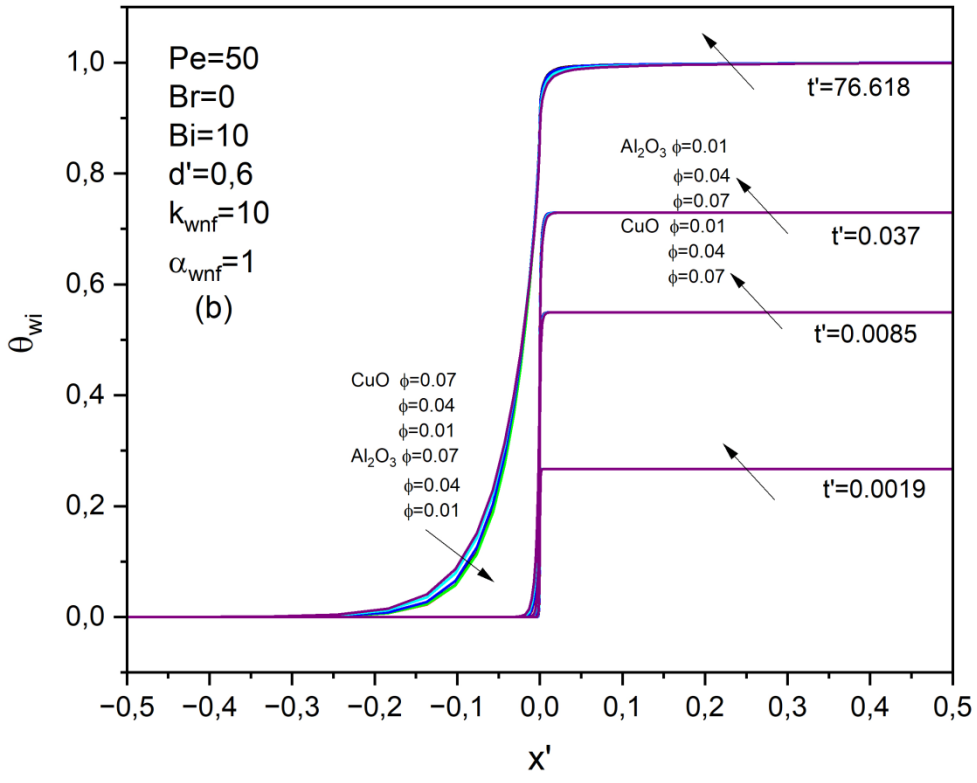


Fig. 2. Axial distribution of transient inner wall temperatures: (a) Pe=5, (b) Pe=50.

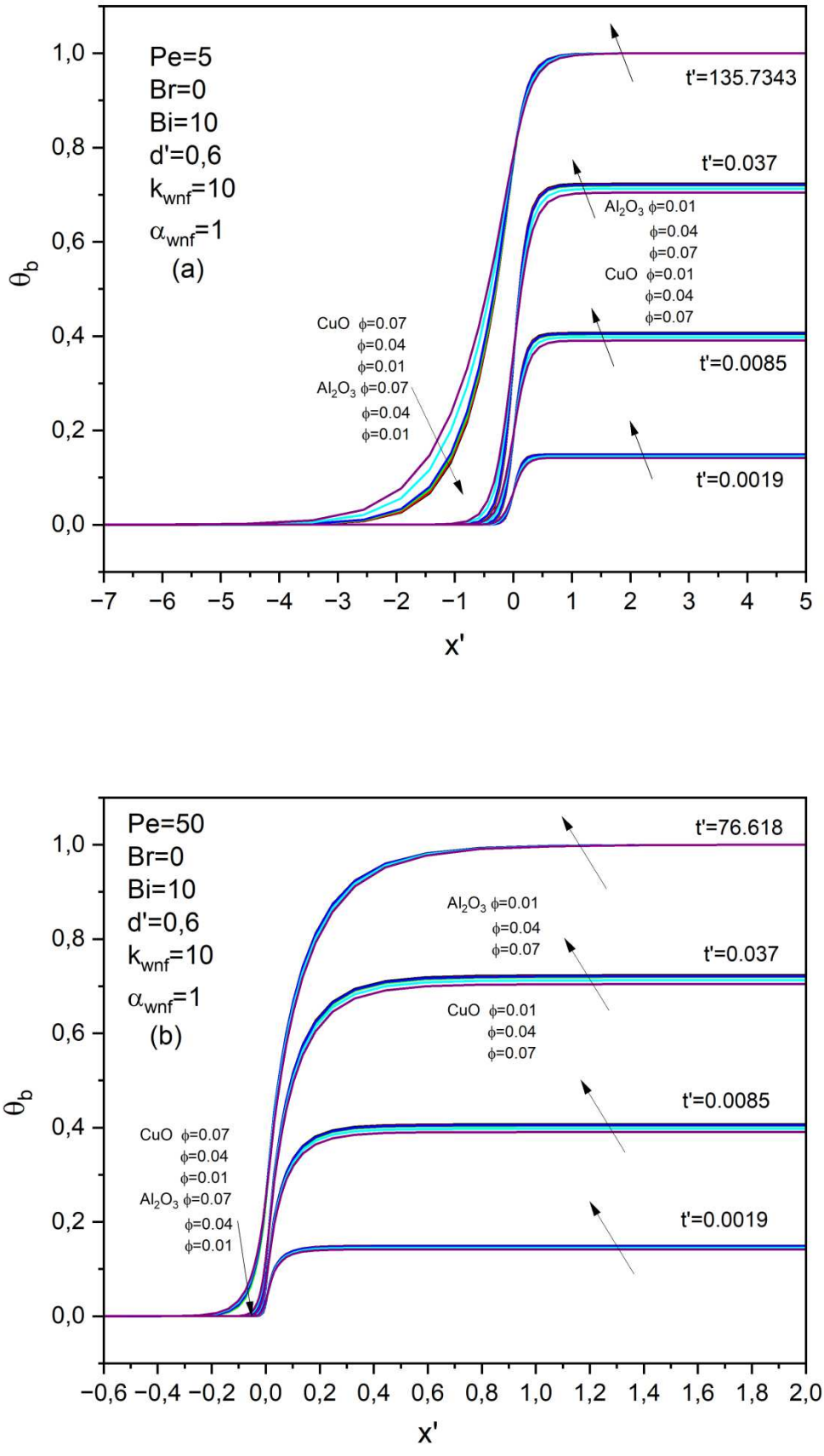
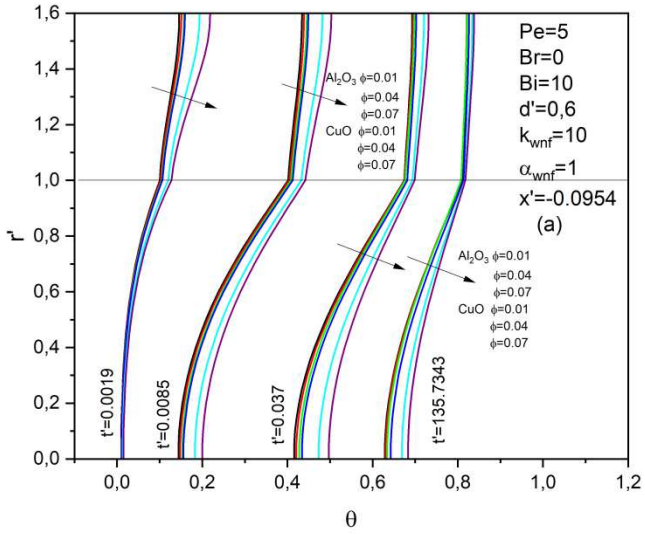
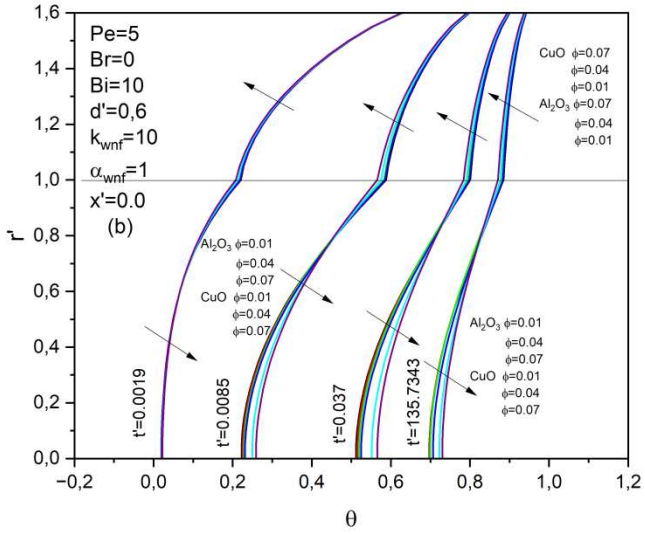


Fig. 3. Axial distribution of transient bulk temperatures: (a) Pe=5, (b) Pe=50.





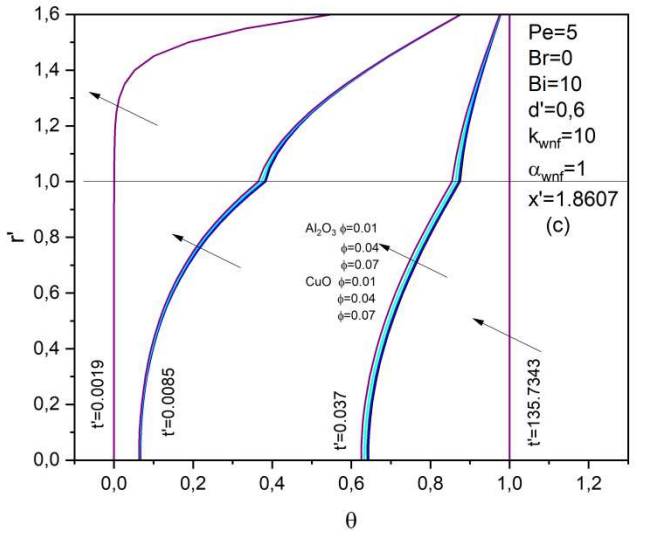
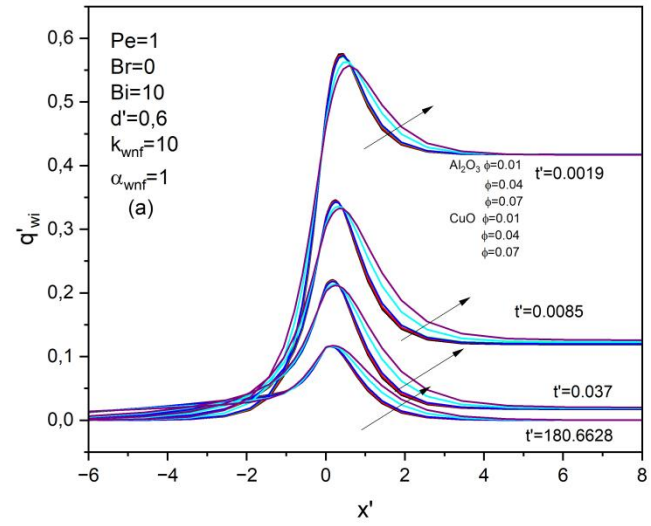
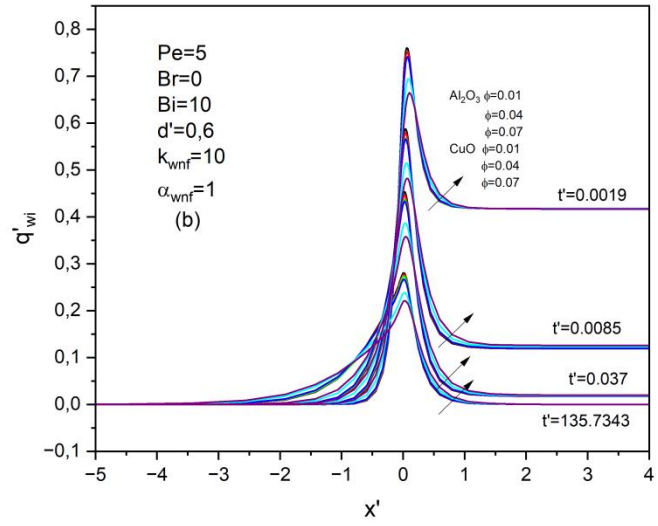


Fig. 4 transient radial distribution of temperatures: (a) x'=-0.0954, (b) x'=0, (c) x'=1.8607.





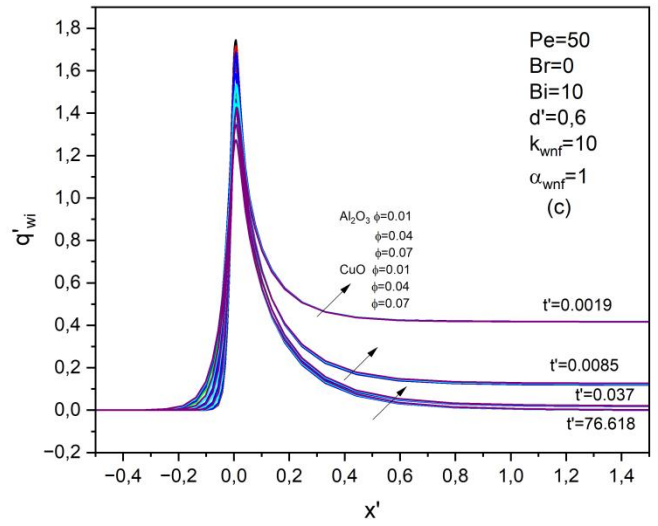


Fig.5 Effect of Peclet number on interfacial heat flux: (a) Pe=1 (b)Pe=5 (c) Pe=50.

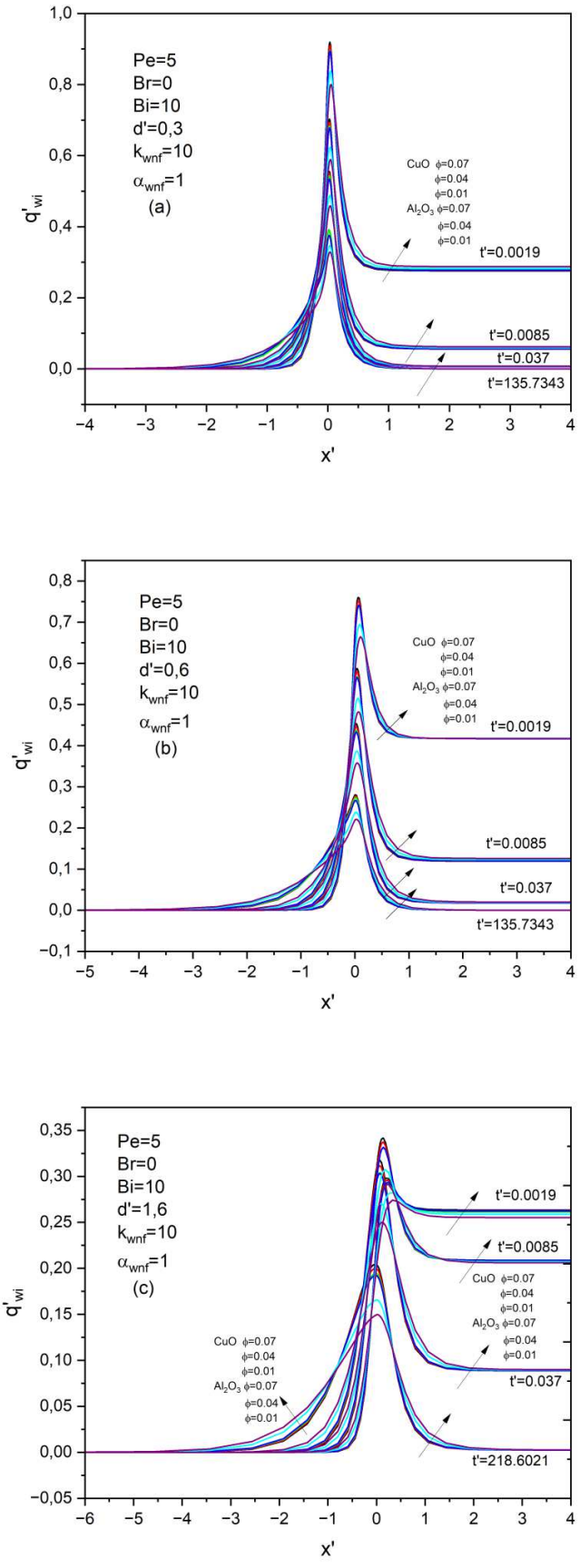


Fig.6 Effect of thickness ratio on interfacial heat flux: (a) d'=0.3, (b) d'=0.6, (c) d'=1.6.

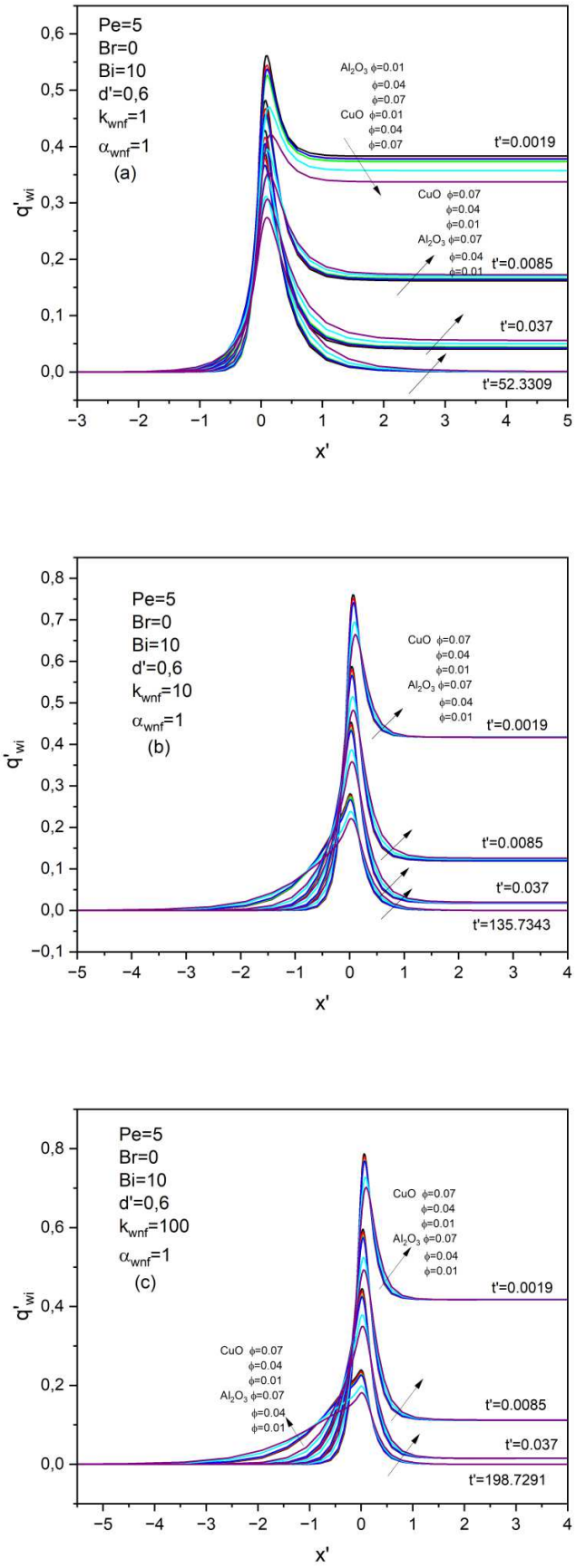


Fig.7 Effect of wall to fluid conductivity ratio on interfacial heat flux: (a) $k_{wnf}=1$, (b) $k_{wnf}=10$, (c) $k_{wnf}=100$.

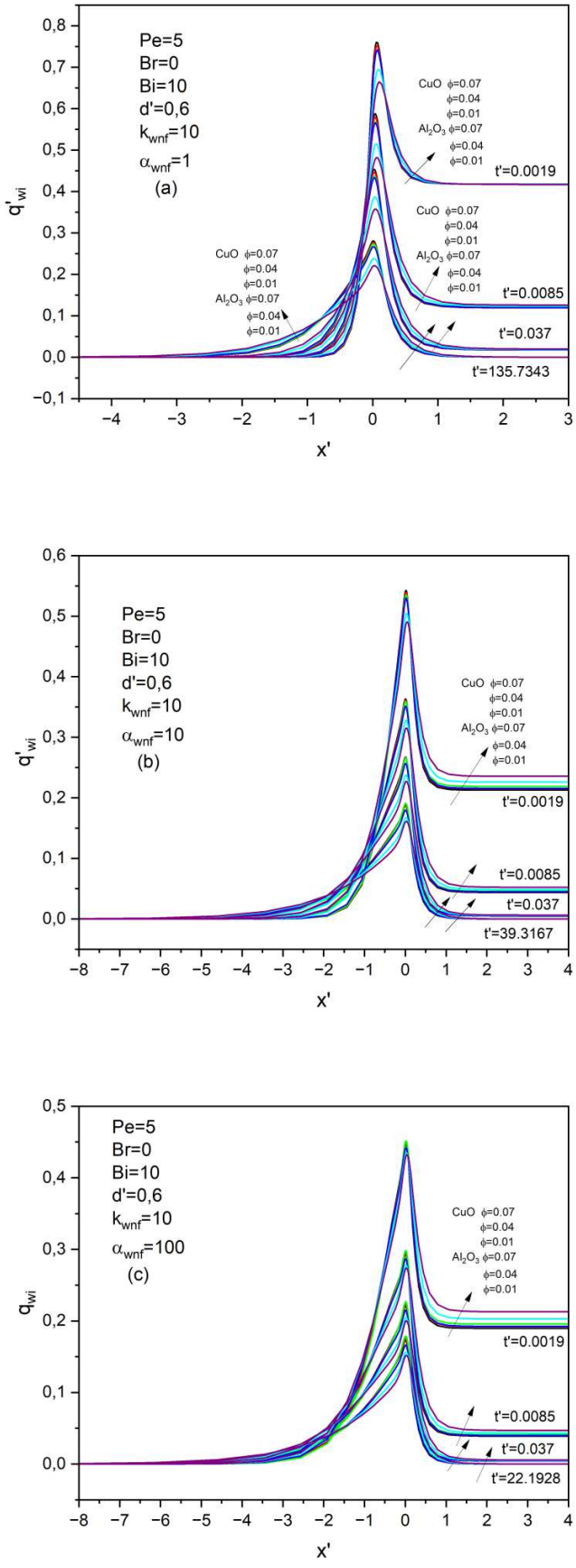


Fig.8 Effect of wall to fluid diffusivity ratio on interfacial heat flux: (a) $\alpha_{wnf}=1$, (b) $\alpha_{wnf}=10$, (c) $\alpha_{wnf}=100$.

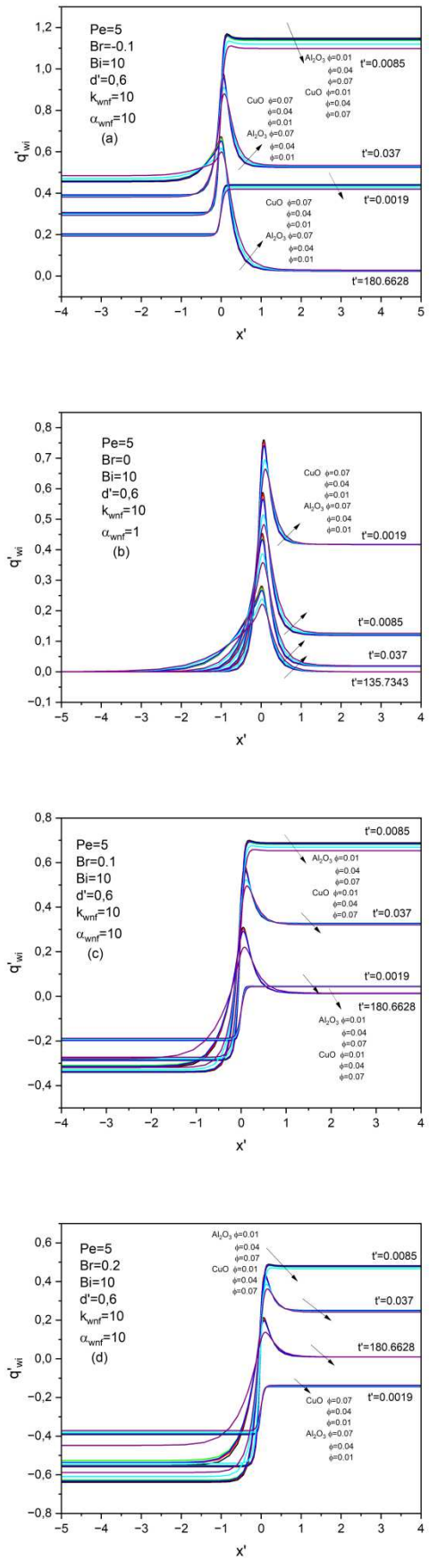


Fig.9 Effect of Brinkman number on interfacial heat flux: (a) Br = -0.1, (b) Br = 0.0, (c) Br = 0.1, (d) Br = 0.2

Conclusions

The effect of nanofluids on laminar flow heat transfer is solved numerically and the effects of seven parameters on thermal characteristic are determined. The findings can be summarized as follows.

There is a substantial amount of heat flux occurring in the upstream region due to both axial conduction in the wall and nanofluid regions. The length of preheating section decreases by increasing Peclet number. The duration for getting steady state decrease as the Peclet number increases.

The effect of nanofluid concentration can be seen clearly at steady state and at upstream region. At the downstream region the bulk temperature values are higher for Al_2O_3 than to CuO.

Preheating length and thermal development length increase considerably by decreasing Peclet number but not affected by the nanofluid concentrations

As the wall thickness increases the peak and interfacial heat flux values decreases and the duration for getting steady state also increases as the wall thickness increases but not affected by the nanofluid concentrations

The duration for reaching steady state also increases with increasing k_{wnf}. The effect of nanofluid concentration can be seen more clearly at lower k_{wnf} values.

The peak and transient heat flux values are greater for lower α_{wnf} values due to increased thermal inertia.

It is seen that, in all time steps the fluid temperatures in the upstream region increase with the increase in viscous dissipation and there is reverse heat flux from fluid to wall side for positive *Br* numbers.

Methods

Modelling Approaches: Single-Phase and Two-Phase Models

Nanofluids can be modelled in two main categories: single-phase and two-phase models. In the single-phase model, the nanofluid is treated as a homogeneous fluid with effective properties derived from the properties of the base fluid and nanoparticles. [9]. This approach simplifies analysis by avoiding the complexity of tracking the individual behaviour of nanoparticles. The second approach, the two-phase model, takes into account the separate phases of the base fluid and nanoparticles, considering their interactions and relative movements. Two-phase models generally predict higher heat transfer coefficients than single-phase models and show better agreement with experimental data, especially for higher nanoparticle concentrations.

Despite its simplicity, the single-phase model can give accurate results under certain conditions. The choice between these models depends on the complexity of the application and the desired level of accuracy; recent studies have more clearly defined the limitations and validity ranges of both models for specific flow regimes and nanoparticle concentrations. [6] Thermal conductivity and viscosity models play a critical role in accurately predicting the behaviour of nanofluids in heat transfer applications. Experimental studies on forced convective heat transfer of Al_2O_3-water and CuO-water nanofluids in square channels under steady heat flux have revealed significant improvements in heat transfer performance. [13].

Governing Equations and Boundary Conditions

The problem discussed in this article has been solved using a single-phase model assumption. Conjugate heat transfer refers to simultaneous heat transfer between solid and fluid regions, where heat conduction in solid structures interacts with convective heat transfer in fluid flow. [14]. In some cases, it is important to determine the heat transfer at the interface where two regions with different thermal properties intersect.

This study numerically investigates a transient conjugate heat transfer scenario within thick-walled micropipes featuring developed laminar flow. The analysis incorporates the effects of two-dimensional wall conduction, axial wall-to-fluid conduction in laminar flow regimes, and viscous dissipation. Key parameters examined include the Peclet number, Brinkman number, wall-to-fluid thermal conductivity ratio, wall-to-fluid thermal diffusivity ratio, wall thickness ratio, and the Biot number.

Initially the whole system is isothermal at temperature of T_o. The flow pipe is assumed as extends infinitely in both ends. The fluid temperature is taken as T_o and uniform at the far upstream. The wall at the upstream side is assumed as insulated. The fluid is developed far away from the starting point of heating. At time *t=0* the ambient temperature of downstream region of wall raises to a value of T_1, and remains constant along the outer wall surface. The schematics and the coordinate system are shown in Fig. 1.

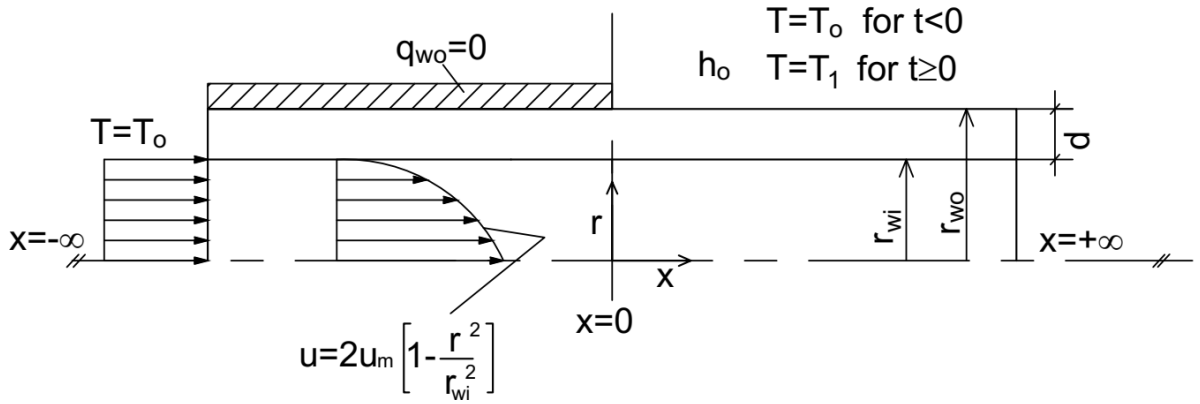


Fig.1. Schematics and the coordinate system of the problem

The problem can be formulated in non-dimensional form as follows. The energy equation in the wall side is,

$$\frac{r'}{\alpha_{wnf}}\frac{\partial\theta_w}{\partial t'}=\frac{\partial}{\partial r'}\left(r'\frac{\partial\theta_w}{\partial r'}\right)+\frac{r'}{Pe^2}\frac{\partial}{\partial x'}\left(\frac{\partial\theta_w}{\partial x'}\right) \quad (1)$$

The initial and boundary conditions are,

at $t'=0$ $\quad \theta_w=0$ (2.a)

at $x'=-\infty$ $\quad \theta_w=0$ (2.b)

at $x'=+\infty$ $\quad \frac{\partial\theta_w}{\partial x'}=0$ (2.c)

at $r'=1$ $\quad \theta_{nf}=\theta_w$ (2.d)

at $r'=1$ $\quad \frac{\partial\theta_w}{\partial r'}=\frac{1}{k_{wnf}}\frac{\partial\theta_{nf}}{\partial r'}$ (2.e)

at $r'=1+d'$ and $for\ x'<0$ $\quad \frac{\partial\theta_w}{\partial r'}=0$ (2.f)

at $r'=1+d'$ and $for\ x'\geq 0$ $\quad \frac{\partial\theta_w}{\partial r'}+Bi\ (\theta_w-1)$ (2.g)

The differential equation for fluid side is

$$r'\frac{\partial\theta_{nf}}{\partial t'}+\left(r'-r'^3\right)\frac{\partial\theta_{nf}}{\partial x'}-\frac{r'}{Pe^2}\frac{\partial}{\partial x'}\left(k'_{wnf}\frac{\partial\theta_{nf}}{\partial x'}\right)=\frac{\partial}{\partial r'}\left(k'_{wnf}r'\frac{\partial\theta_{nf}}{\partial r'}\right)+16\,Br\,r'^3 \quad (3)$$

The initial and boundary conditions are,

At $t^{'} = 0$ $\theta_{nf} = 0$ (4.a)

At $x^{'} = -\infty$ $\theta_{nf} = 0$ (4.b)

At $x^{'} = \infty$ $\frac{\partial \theta_{nf}}{\partial x^{'}} = 0$ (4.c)

At $r^{'} = 0$ $\frac{\partial \theta_{nf}}{\partial r^{'}} = 0$ (4.d)

At $r^{'} = 1$ $\theta_{nf} = \theta_{w}$ (4.e)

At $r^{'} = 1$ $\frac{\partial \theta_{nf}}{\partial r^{'}} = k_{wnf} \frac{\partial \theta_{w}}{\partial r^{'}}$ (4.f)

The non dimensional parameters of the problem are,

$\theta = \frac{T - T_o}{T_1 - T_o}$, $x^{'} = \frac{x}{r_w \, Pe} = \frac{2}{Gz}$, $r^{'} = \frac{r}{r_w}$, $d^{'} = \frac{d}{r_w}$, $k_{wnf} = \frac{k_w}{k_{nf}}$, $\alpha_{wnf} = \frac{\alpha_w}{\alpha_{nf}}$,

$t^{'} = \frac{t \, \alpha_f}{r_{wi}^2} = Fo$ $Pe = \mathrm{Re} \cdot \mathrm{Pr} = \frac{2 r_{wi} u_m (\rho c_p)_{nf}}{k_{nf}}$, $\mathrm{Br} = \frac{\mu_{nf} u_m^2}{k_{nf}(T_1 - T_o)}$, $Bi = \frac{h \, r_{\mathrm{wi}}}{k_{\mathrm{w}}}$

Non dimensional fluid bulk temperature, θ_b, interfacial heat flux, $q_{wi}^{'}$, and local Nusselt numbers, *Nu*, can be calculated as,

$\theta_b = 4 \int_0^1 r^{'} \left(1 - r^{'2}\right) \theta_{nf} dr^{'}$ (5)

$q_{wi}^{'} = -\left(\frac{\partial \theta_{nf}}{\partial r^{'}}\right)_{r^{'}=1}$ (6)

$Nu = \frac{-2 q_{wi}^{'}}{\theta_{wi} - \theta_b}$ (7)

Properties of the Nanofluids

It is assumed that the nanoparticles are well dispersed within the base fluid and form a homogeneous mixture and it is considered as a single-phase nanofluid. The thermophysical properties can be given as follows. The density and the thermal capacitance of the nanofluid are [10];

$\rho_{nf} = (1 - \phi)\rho_f + \phi \rho_p$ (10)

$\left(\rho C_p\right)_{nf} = (1 - \phi)\left(\rho C_p\right)_f + \phi \left(\rho C_p\right)_p$ (11)

The thermal conductivity of the nanofluid is [15] , the thermal conductivity plays a dominant role for obtaining heat transfer characteristics of nanofluid [16].

$k_{\mathrm{nf}} = \left\{ \frac{[k_{\mathrm{p}} + (n-1)k_{\mathrm{f}} - (n-1)(k_{\mathrm{f}} - k_{\mathrm{p}})\phi]}{[k_{\mathrm{p}} + (n-1)k_{\mathrm{f}} + (k_{\mathrm{f}} - k_{\mathrm{p}})\phi]} \right\} k_{\mathrm{f}}$ (12)

The thermophysical properties of the nanoparticles are given in Table 1 ([17]and [18])

Table 1. Properties of nanoparticles and basefluid

	ρ	**C_p**	**k**
Base fluid(water)	998.2 kg/m3	4182 J/kg°C	0.597 W/m°C
Al_2O_3	3880 kg/m^3	773 J/kg°C	36 W/m°C
CuO	6320 kg/m^3	531.8 J/kg°C	76.5W/m°C

Solution Methodology

The energy equations are solved simultaneously by a numerical finite difference method. The conductivity terms are discretized by central difference method while the convective terms are discretized by a exact method defined by [19]. This method is a version of exact or exponential scheme defined by Patankar [20].

The following equation is obtained for nodal points (*i,j*)

$$A_{i,j}\theta_{i,j} = A_{i+1,j}\,\theta_{i+1,j} + A_{i-1,j}\,\theta_{i-1,j} + A_{i,j+1}\,\theta_{i,j+1} + A_{i,j-1}\,\theta_{i,j-1} + A^0_{i,j}\theta^0_{i,j} + D \tag{8}$$

where in the nanofluid side;

$$A_{i+1,j} = \frac{\left(r'_{i,j} - r'^3_{i,j}\right)\Delta r'_{i,j}}{exp\left[Pe^2\left(1-r'^2_{i,j}\right)\frac{\delta x'_{i+1,j}}{k'_{wnf}}\right]-1} \tag{9.a}$$

$$A_{i-1,j} = \frac{\left(r'_{i,j} - r'^3_{i,j}\right)\left(exp\left[Pe^2\left(1-r'^2_{i,j}\right)\frac{\delta x'_{i-1,j}}{k'_{wnf}}\right]\right)\Delta r'_{i,j}}{exp\left[Pe^2\left(1-r'^2_{i,j}\right)\frac{\delta x'_{i-1,j}}{k'_{wnf}}\right]-1} \tag{9.b}$$

$$A^0_{i,j} = \frac{r_{i,j}'(\Delta x')_{i,j}\,(\Delta r')_{i,j}}{\Delta t'} \tag{9.c}$$

$$D = 16\,Br\,r'^3_{i,j}(\Delta r')_{i,j}\,(\Delta x')_{i,j} \tag{9.d}$$

In the wall side

$$A_{i+1,j} = \frac{r'_{i,j}\,\Delta r'_{i,j}}{Pe^2\,\delta x'_{i+1,j}} \tag{9.e}$$

$$A_{i-1,j} = \frac{r'_{i,j}\,\Delta r'_{i,j}}{Pe^2\,\delta x'_{i-1,j}} \tag{9.f}$$

$$A^0_{i,j} = \frac{r_{i,j}'}{\alpha_{wnf}}\frac{(\Delta x')_{i,j}\,(\Delta r')_{i,j}}{\Delta t'} \tag{9.g}$$

and in both sides,

$$A_{i,j+1} = \frac{r'_{i,j+1}\,\Delta x'_{i,j}}{\delta r'_{i,j+1}} \tag{9.h}$$

$$A_{i,j-1} = \frac{r'_{i,j-1}\,\Delta x'_{i,j}}{\delta r'_{i,j-1}} \tag{9.i}$$

$$A_{i,j} = A_{i+1,j} + A_{i-1,j} + A_{i,j+1} + A_{i,j-1} + A^{0}_{i,j} \tag{9.j}$$

The computational domain is discretized using a grid system applied to both the nanofluid and wall regions. Uniform spacing is maintained in the radial direction, with grid points clustered near the initiation of the heating section. In the axial direction, the initial grid spacing is set to 0.001 for both upstream and downstream sections, with subsequent grids expanding by 34% of the preceding distance. The mesh consists of 12 divisions in the wall region and 20 in the nanofluid region, with 38 axial grids distributed across both upstream and downstream segments. The time discretization is also non-uniform, starting with a step of 0.0001 and increasing by 10% for subsequent steps. Temperature fields are resolved using the Gauss-Siedel iterative technique. Within each time step, iterations proceed radially from the outer pipe surface towards the axis and sweep axially from upstream to downstream. Boundary conditions are discretized using a harmonic mean formulation [20]. Information transfer between the wall and fluid, and vice versa for interfacial heat flux, is facilitated by utilizing previously calculated temperature values during the iterative process. Convergence is achieved when the solution stabilizes within a tolerance of 10^{-6}. Grid independence was verified through generalized Richardson extrapolation and the grid convergence index method, as proposed by Roache[21]. Comparisons were made between coarse and fine grid solutions, with a grid refinement ratio of 1.32. Interfacial heat flux and temperature values at steady state at the beginning of the heated section were evaluated. The parameter values utilized in these calculations are presented in Table 2. These results indicate that the chosen grid resolution is adequate and further refinement is not necessary.

Table 2. Effect of grid size on T'_{wi} and q'_{wi}

steady state values at x′=0	axial grid		radial grid	interfacial temperature (T'_{wi})	Interfacial heat flux , q'_{wi}
	upstream region	downstream region			
Pe=5, d^{*}=0.6, k_{nwf}=10, α_{nwf}=1, Bi=10, Br=0					
fine grid	50	50	44	0.61837	0.28120
medium grid	38	38	34	0.61764	0.28054
coarse grid	26	26	26	0.61549	0.30837
∈ between medium and coarse grids(%)				0.001182	0.00234708
GCI between medium and coarse grids (%)				0.000759	0.00007119
∈ between fine and medium grids (%)				0.003481	-0.0992015
GCI between fine and medium grids (%)				0.002237	0.00301

Nomenclature

A constant of discretization equation (Eq. 8)
Bi Biot number
Br Brinkman number
c_p specific heat at constant pressure
Fo Fourier number

Gz Graetz number
h film coefficient
Pe Peclet number
Re Reynolds number
Pr Prandtl number
k thermal conductivity
r radial coordinate
L length
T temperature
u axial velocity
x axial coordinate
q heat flux
t time
T temperature
Nu Nusselt number
D source term

Greek symbols

α thermal diffusivity
ϕ nanofluid concentration
δr radia position difference
δx axial position difference
Δr radial step size
Δt time step increment
Δx axial step size
θ temperature
ρ density
μ dynamic viscosity

Subscripts

b bulk
i inner wall
nf nanofluid
m mean
f base fluid
h heated length
wnf wall to nanofluid
p particle
φ volume fraction
i,j at nodal point *i,j*
w wall

Superscripts

' dimensionless quantity
o at previous time step

Greek symbols

θ dimensionless temperature
ρ density

Data Availability Statement

The numerical data (in-house finite-difference code and generated datasets) that support the findings of this study are available from the corresponding author upon reasonable request.

References

1. Choi, S.U.S., *Enhancing thermal conductivity of fluids with nanoparticles.* Developments and Applications of Non-Newtonian Flows, FED, 1995. **231** (66): p. 99-105.
2. Vajjha, R.S. and D.K. Das, *A review and analysis on influence of temperature and concentration of nanofluids on thermophysical properties, heat transfer and pumping power.* International Journal of Heat and Mass Transfer, 2012. **55** (15): p. 4063-4078.
3. Saoudi, L., & Zeraibi, N., *Entropy generation of Al2O3/water nanofluid in corrugated channels.* Journal of Thermal Engineering, 2023. **9** (4): p. 885-900.
4. Ganvir, R.B., P.V. Walke, and V.M. Kriplani, *Heat transfer characteristics in nanofluid—A review.* Renewable and Sustainable Energy Reviews, 2017. **75**: p. 451-460.
5. Kaggwa, A. and J.K. Carson, *Developments and future insights of using nanofluids for heat transfer enhancements in thermal systems: a review of recent literature.* International Nano Letters, 2019. **9** (4): p. 277-288.
6. Kamyar, A., R. Saidur, and M. Hasanuzzaman, *Application of Computational Fluid Dynamics (CFD) for nanofluids.* International Journal of Heat and Mass Transfer, 2012. **55** (15): p. 4104-4115.
7. Trisaksri, V. and S. Wongwises, *Critical review of heat transfer characteristics of nanofluids.* Renewable and Sustainable Energy Reviews, 2007. **11** (3): p. 512-523.
8. Wang, X.-Q. and A.S. Mujumdar, *Heat transfer characteristics of nanofluids: a review.* International Journal of Thermal Sciences, 2007. **46** (1): p. 1-19.
9. Hussain, M.I., Kim, J., & Kim, J.-T. (*Nanofluid-Powered Dual-Fluid Photovoltaic/Thermal (PV/T) System: Comparative Numerical Study.* Energies, 2019. **12** (5): p. 775.
10. Maïga, S.E.B., et al., *Heat transfer behaviours of nanofluids in a uniformly heated tube.* Superlattices and Microstructures, 2004. **35** (3): p. 543-557.
11. Narankhishig, Z., et al., *Convective heat transfer characteristics of nanofluids including the magnetic effect on heat transfer enhancement - a review.* Applied Thermal Engineering, 2021. **193**: p. 116987.
12. Ilker Goktepeli, U. Atmaca., *Comparison of Thermophysical Property Models of Nanofluids for Thermal Performance in a Microchannel.* Heat Transfer Research, 2025. **56** (2): p. 1-15.
13. Nassan, T.H., Heris, S. Z., & Bagheban, S. H. N., *Experimental Investigation of nanofluid heat transfer in a square cross-sectional duct.* arXiv (Cornell University), 2023.
14. Borode, A., Ahmed, N. A., & Olubambi, P. A., *Application of Carbon-based Nanofluids in Heat Exchangers: Current Trends. .* Journal of Physics Conference Series, 2019. **1378** (32061).
15. Hamilton, R.L. and O.K. Crosser, *Thermal Conductivity of Heterogeneous Two-Component Systems.* Industrial & Engineering Chemistry Fundamentals, 1962. **1** (3): p. 187-191.
16. Nimmagadda, R. and K. Venkatasubbaiah, *Conjugate heat transfer analysis of micro-channel using novel hybrid nanofluids (Al_2O_3+Ag/Water).* European Journal of Mechanics - B/Fluids, 2015. **52**: p. 19-27.
17. Pak, B.C. and Y.I. Cho, *Hydrodynamic and Heat Transfer Study of Dispersed Fluids with Submicron Metallic Oxide Particles.* Experimental Heat Transfer, 1998. **11** (2): p. 151-170.
18. Alloui, Z., P. Vasseur, and M. Reggio, *Natural convection of nanofluids in a shallow cavity heated from below.* International Journal of Thermal Sciences, 2011. **50** (3): p. 385-393.
19. Bilir, Ş., *Numerical Solution of Graetz Problem with Axial Conduction.* Numerical Heat Transfer, Part A: Applications, 1992. **21** (4): p. 493-500.
20. Suhas, P., *Numerical Heat Transfer and Fluid Flow (1st ed.).* 1980.
21. Roache, P.J., *Perspective: A Method for Uniform Reporting of Grid Refinement Studies.* Journal of Fluids Engineering, 1994. **116** (3): p. 405-413.
22. Singh, V., & Gupta, M. K., *Characterisation and Zeta Potential Measurements of CuO–Water Nanofluids.* Springer Nature, Lecture notes in mechanical engineering 2019: p. 741.

23. Singh, V., Gupta, M. K., & Kumar, A. , *Investigating the morphology and thermophysical properties of Al2O3 and CuO nanofluids.* IOP Conference Series Materials Science and Engineering, 2019. **577** (1).

Acknowledgements

This paper is based on the dissertation work of the first author. This work received no specific grant from any funding agency in the public, commercial, or not-for-profit sectors.

Author Contributions

I.M.A.R.R. developed the numerical solver, performed the simulations, and analysed the data. U.A. conceived and supervised the study, contributed to the interpretation of results, and revised the manuscript. Both authors reviewed and approved the final manuscript.

Competing Interests

No potential conflict of interest was reported by the author(s).